# Precipitation resonance for an idealized ITCZ model

**Jan O. Haerter [1,2,3] and Romain Fiévet [3]**

[1]Complexity and Climate, Leibniz Center for Tropical Marine Research, Fahrenheitstrasse 6, 28359 Bremen, Germany
[2]Jacobs University Bremen, Campus Ring 1, 28759 Bremen, Germany
[3]Niels Bohr Institute, University of Copenhagen, Blegdamsvej 17, 2100 Copenhagen, Denmark

## Key Points:

- The diurnal cycle interacts with the large scale circulation,
- The diurnal period becomes dominant for system sizes smaller than $\approx 2000\,km$,
- The interaction can be conceptually modeled by a forced oscillator with a self-drive.

Corresponding author: Jan O. Haerter, `haerter@nbi.ku.dk`

## Abstract

Tropical convection is known to self-organize under the diurnal cycle, yet is also subject to large scale convergence. In a suite of idealized numerical experiments we mimic Earth's tropical circulation, to probe the cross talk between inherent circulation eigenmodes and the convective diurnal cycle — which generally are characterized by incommensurate oscillatory frequencies. The tropics are caricatured by a doubly-periodic domain with spatially constant surface temperature $T_S(x, y, t)$ in the "zonal" ($x$) but decreasing $T_S$ in the "meridional" dimension. Temporally, we contrast constant $T_S(x, y, t) = T_S(x, y)$ with diurnally varying $T_S(x, y, t) = T_S(x, y, t + \tau_d)$, with $\tau_d = 1$ day. We find that the diurnal forcing by no means dominates the precipitation power spectrum. Rather, the intrinsic circulation period $\tau_i$ drives temporal precipitation patterns for large and small domains. At intermediate domain sizes, where intrinsic frequencies approximately match the diurnal one, i.e., $\tau_i \approx \tau_d$, the diurnal cycle is amplified and, substantially increasing the precipitation amplitude.


## 1 Introduction

Tropical large scale atmospheric circulations and local scale moist convection have proven to be intrinsically coupled, such as for the Hadley Cell and intertropical convergence zone (ITCZ) as well as the Madden-Julian Oscillation (MJO). The interaction between circulation patterns and convection has been extensively studied within a range of simplified models (Lindzen, 1974; K. A. Emanuel, 1987; Neelin et al., 1987; Wang, 1988; Takayabu, 1994; Wheeler & Kiladis, 1999; Kiladis et al., 2009; Mapes, 2000; Majda & Shefter, 2001; Sobel & Bretherton, 2000; Härtel et al., 2000; Kuang, 2012; Yang & Ingersoll, 2013; Yang, 2021). Many of these works use a form of linearized shallow water equations, yet, coupling to moist convection, itself a threshold effect, preserves an essential, strong non-linearity. The intriguing notion that convection is both a result and a cause of the large scale circulation is central to many of these studies. Specifically, the large-scale low-level moisture convergence can give rise to convection and the tropospheric heating, caused by cloud formation, is the cause of a circulation. Despite this tremendous body of research, even basic features of the coupling of cumulus convection to the large-scale circulation remain poorly understood, e.g, the MJO continues to be the subject of a range of plausible theories (Zhang et al., 2020).

A prevailing, yet not conclusively explained, finding in models allowing for self-organization of convectively-coupled equatorial waves is that, in the steady state, a low-wavenumber mode is typically excited, whereas higher wavenumbers are less dominant. As a case in point, analysis of two-dimensional cloud system resolving equatorial wave simulations Tulich, Randall, and Mapes (2007), run to radiative convective equilibrium, illustrated that a low-wavenumber mode with propagation speed of 16 to 18 $m\,s^{-1}$ appeared to dominate. It is thus intriguing to seek simplified models that explain why large wavelength modes are "picked out" by emergent organization in coupled circulation-convection atmospheres. One promising candidate theory is that by Yang and Ingersoll (2013), where the shallow water equations are coupled to a simple, threshold based, representation of convective heating. In their model, high-frequency convective activity is able to excite low-frequency standing gravity waves, by which the tropical atmosphere self-organizes to a climatological steady state. One of the authors recently applied the model to convective self-aggregation (Yang, 2021).

Spatially and temporally varying boundary conditions have been applied to excite oscillations in the circulation patterns. To mimic the MJO Yamagata and Hayashi (1984) incorporated 40-day periodic SST forcing into a simple model, which then resulted in a standing wave for zonal wind. Forcing with diurnally-varying SST, recent work found deep convection to strongly organize into mesoscale convective systems, which tend to anticorrelate from one day to the next (Haerter et al., 2020) but can give rise to persistent dry patches at longer timescales (Jensen et al., 2021). Spatial SST gradients are known to lead to convective organization effects (Tompkins, 2001; Kuang, 2012; Shamekh et al., 2020), where regions of larger SSTs were found to align with increased mean precipitation rates.

Yet, even without any boundary condition structure, convective self-organization can bring about system-scale circulations. A prominent case is convective self-aggregation (Held et al., 1993; Bretherton et al., 2005; C. J. Muller & Held, 2012; K. Emanuel et al., 2014; Patrizio & Randall, 2019; Wing & Cronin, 2016; C. Muller et al., 2022), which, once formed, is likely maintained by a complex feedback between cloud, radiation and the large scale circulation, a mechanism that was also invoked highly-idealized simulations of the Hadley Cell (Raymond, 2000). For varying horizontal domain sizes under homogeneous surface boundary conditions Patrizio and Randall (2019) find that system-scale emergent circulations exhibit low-frequency oscillations in domain-mean precipitation or outgoing longwave radiation (OLR). Imposing meridional sea surface temperature gradients for idealized aquaplanets, Müller and Hohenegger (2020) demonstrated that self-aggregation effects can even be strong enough to overwhelm the forced Hadley Cell type circulations. In recent work (Yang, 2021), the coupling between linear gravity waves and short-lived moist convection was suggested as a means of obtaining convective self-aggregation.

In the current work, we focus on timeseries of tropical precipitation, which serve as a signature of the large scale circulation. We address the question of how an intrinsic large-scale idealized Hadley Cell circulation is perturbed, when interacting with the — temporally periodic — diurnal cycle. The former is established by imposing a spatial large-scale surface temperature gradient, leading to a low-level moisture convergence near the model equator. The latter is introduced by allowing for a diurnal variation of surface temperature throughout the domain. We find that, generally, in the steady state, both the intrinsic (termed $\omega_0$) and diurnal (termed $\Omega$) frequency contribute. However, when $\omega_0 \approx \Omega$, a form of resonance is found where oscillations are locked in with the diurnal cycle. When frequencies differ sufficiently the spectral weight of the diurnal cycle is almost negligible. We construct a simple conceptual model which builds on a simple linear harmonic oscillator, but incorporates a nonlinear convective feedback to induce a blend of frequencies.

## 2 Numerical Methods

### 2.1 Cloud-resolving model

All numerical simulations carried out in the study use the *System for Atmospheric Modeling* (SAM) cloud-resolving model (Khairoutdinov & Randall, 2003), version 6.11. The model resolves an anelastic form of the Navier-Stokes equation over a fully staggered Arakawa C-type grid with stretched vertical and uniform horizontal meshes. Numerical fluxes are calculated using the fifth-order finite difference scheme from (Yamaguchi et al., 2011) and the solution is explicitly integrated in time with a third-order Adams-Bashforth scheme. On top of the fluid conservative variables, the prognostic variables include the liquid/ice water static energy, the total precipitating and nonprecipitating water. In order to alleviate computational costs, subgrid turbulence and microphysics parameterizations simply consist in, respectively, Smagorinsky-Lilly and single-moment closure models. Radiative fluxes are evaluated using the Rapid Radiative Transfer Model (RRTM) (Mlawer et al., 1997), with a diurnal top-of-the-atmosphere shortwave flux peaking to 1350 $W/m^2$ at midday. Surface fluxes are computed using Monin–Obukhov similarity using a prescribed sea surface temperature (SST) profile. A diurnal cycle can be imposed in the form of top-of-the-atmosphere shortwave forcing with a sea surface temperature oscillation.

| Case | $L_y$ $[10^3 km]$ | $\Delta T_y\,[K]$ | Type of runs | $\Delta t\,[days]$ |
|---|---|---|---|---|
| 1 | 1 | 10 | Spin-up, RCE, DIU | 30 |
| 2 | 2 | 10 | Spin-up, RCE, DIU | 30 |
| 3 | 4 | 10 | Spin-up, RCE, DIU | 30 |
| 4 | 4 | 5 | Spin-up, RCE, DIU | 30 |
| 5 | 4 | 2.5 | Spin-up, RCE | 30 |
| 6 | 4 | 0 | Spin-up, RCE | 30 |
| 7 | 4 | 10 | BI-DIU (Forcing period: $48h$) | 30 |
| 8 | 8 | 10 | Spin-up, RCE, DIU | 30 |

**Table 1. Summary of numerical experiments.**

### 2.2 Domain configuration

This numerical study comprises eight different cases presented in Tab. 1. Each case represents an idealized tropical ocean of domain size $L_x \times L_y \times L_z$, with $x$, $y$ and $z$ denoting *longitude*, *latitude* and *altitude* coordinates, respectively. For all cases, $L_x = 2,000$ km and $L_z = 27$ km with horizontal mesh resolution $\Delta x = 4$ km and vertical resolution $\Delta z$ stretching from 50 m at the first level ($z = 25$) to 716 m at the top of the atmosphere. This amounts to a total of 64 vertical levels. Cases differ in the setting of $L_y$, which progressively increases from 1,000 to 8,000 km (Tab. 1).

The spatiotemporal mean SST is set to $T_0 = 298$ K. To mimic the Intertropical Convergence Zone (ITCZ), a latitudinal SST gradient $\Delta T_y$ is imposed as a half sinusoidal function of range $\Delta T_y$. Finally, several simulations study the influence of the diurnal cycle which is modeled as an additional sinusoidal SST forcing of amplitude $\Delta T_t = 2.5$ K. The forcing period $\tau_d = 1d$, except for run 7 which considers a bi-diurnal forcing ($\tau_d = 2d$). Together, the surface temperature $T_S(x, y, t)$ reads:

$$T_S(x, y, t) = T_0 + \Delta T_y \cos\left(\frac{\pi y}{L_y}\right) - \Delta T_t \cos\left(\frac{2\pi t}{\tau_d}\right) \tag{1}$$

Hence, the SST is independent of $x$, and peaks along $y = 0$ (the model *equator*) and at midday if the diurnal cycle is activated. The SST range $\Delta T_y$ is often set to 10 K, but subject to variation in the ($L_y = 4,000$ km)-configuration (cases 3—7). Overall, SST gradients are varied by either modifying the amplitude $\Delta T_y$ or the latitudinal domain size $L_y$. The influence of the diurnal cycle is investigated by contrasting runs with constant SST, which have $\Delta T_t = 0$ and are denoted "RCE", and runs with diurnally oscillating SST, which have $\Delta T_t = 2.5$ K and are denoted "DIU" (*compare*: Tab. 1). For RCE also the top-of-the-atmosphere radiative flux is set constant, to a value equal to the diurnal average. Each of these runs is preceded by a 30 day-long run, termed "spin up," using the RCE configuration to reduce the transient response resulting from the idealized initialization (domain-averaged soundings corresponding to an equilibrated $T_s = 298K$ reference case). After the spin-up the simulation branches into the RCE and DIU runs.

## 3 Results

To analyze the effect of the diurnal cycle on the meridional circulation, we first discuss spatially-averaged timeseries (Sec. 3.1), before we explore more detailed spatio-temporal dynamics (Sec. 3.2) and finally offer a simplified conceptual model for the observed oscillatory pattern.

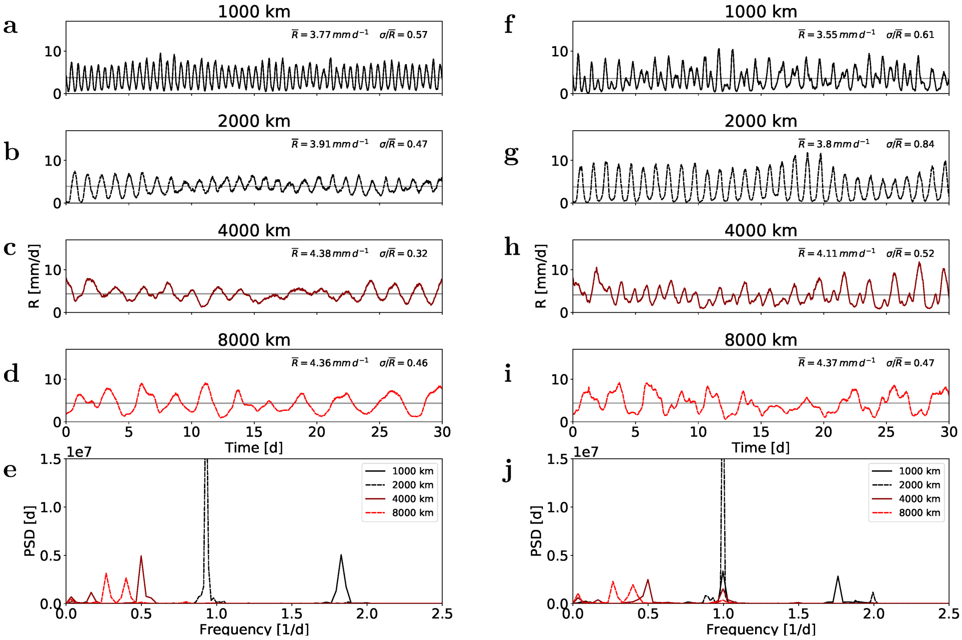


**Figure 1. The effect of the diurnal cycle on precipitation variability.** Timeseries of horizontal-mean surface precipitation intensity for variable meridional domain sizes $L_y$ as labeled on top of each panel for the 30-day analysis period. The latitudinal temperature difference $\Delta T_{s,lat} = 10\,K$ in all simulations shown. **a**—**e**, Simulations corresponding to RCE. **f**—**j**, Simulations corresponding to DIU.

## 3.1 Domain-mean precipitation dynamics

The imposed meridional temperature gradient leads to the rapid organization of the modeled circulation into an ITCZ-like, approximately zonally-symmetric, circulation pattern: pronounced horizontal convergence forms near the meridional surface temperature peak, the "equator," with associated mean rising air masses and deep convective activity. Outside of this band, which stretches several hundred kilometers in the meridional direction, the atmosphere is dominated by subsidence, intermittent shallow convection and nearly rainfree conditions.

The full (3+1)-dimensional spatio-temporal dynamics is complex. Yet, a substantial simplification of the overall precipitation dynamics is achieved by considering the timeseries of horizontally-averaged surface precipitation intensity $R(t) \equiv \langle R(x,y,t)\rangle_{x,y}$, where the subscript denotes the horizontal average over $x$ and $y$ and $R(x,y,t)$ is the surface precipitation field. For later use we also introduce the spatio-temporal rainfall average $\overline{R} \equiv \langle R(x,y,t)\rangle_{x,y,t}$. As mentioned (Sec. 2), for each numerical experiment (Tab. 1) a 60-day period is simulated, which we split into an initial 30-day "spin-up" and a subsequent 30-day "analysis" period. We first fix the meridional extent to $L_y = 4,000\,km$ and examine the sensitivity to the meridional temperature range, $\Delta T_y$, which is varied between zero and ten kelvins (Fig. S1). The surface temperature is here set constant in time. Despite the time-independent surface temperature boundary condition, the timeseries of $R(t)$ is highly variable: during both the spin-up and analysis period pronounced oscillatory dynamics is clearly visible (panels a—d).

To analyze the typical oscillations, we compute the power spectra for each value of $\Delta T_y$ (Fig. S1e), we find that for each of the cases with $\Delta T_y > 0$, and for either of the two 30-day periods, the frequency of oscillation is very similar, $f_0 \approx .5\,d^{-1}$. In all these cases, the domain quickly organizes into the general Hadley Cell-like pattern, with an ITCZ-like convergence area near $y = 0$. The case of $\Delta T = 0K$, which is similar to a classical radiative-convective equilibrium setup, deserves a comment: since the horizontal translational symmetry is here not broken by the surface temperature boundary condition, all organization is purely emergent, that is, self-organized. Indeed, already during the first 30-day period, spatial organization, typical of the early stages of convective self-organization, is present, featuring characteristic emergent dry spots, which gradually expand over time. During the second 30-day period, these dry patches further expand and merge, such that eventually only two larger convective regions remain, each performing time-periodic oscillations. For the spatial domain average $R(t)$ these oscillations are recognizable as an overall temporal oscillation (panels d). Examining the power spectrum, it becomes apparent that the dominant frequency is now somewhat larger, $f_0 \approx .7\, d^{-1}$, than for the finite $\Delta T_y$ cases.

Note also the changes in overall mean precipitation, which increases consistently with the larger meridional temperature gradient. We mainly attribute such changes in mean precipitation to water vapor increases according to the (roughly exponential) Clausius-Clapeyron relation, which would disproportionately favor cases of stronger temperature variance, allowing for overall larger precipitation rates. We however note that in self-aggregation studies, temporally and spatially averaged surface precipitation $\overline{R}$ has often been reported to increase with increased aggregation (Bretherton et al., 2005), which was attributed to enhanced upper tropospheric radiative cooling as a consequence of increased outgoing thermal radiation in the very dry subsidence regions. Indeed, during the second 30-day period, where the case of $\Delta T = 0K$ features pronounced self-aggregation, the rainrate shows an increasing trend.

This exploration of $\Delta T_y$ allows us to assume that the oscillatory period does not depend strongly on the spatial temperature gradient. We now thus to varying domain size $L_y$. Consider first the RCE case (Fig. 1a—e), where sustained oscillations are apparent in all experiments. It is also obvious that the dominant frequency of oscillation, seen in the global power spectral maxima (Fig. 1e), systematically decreases with $L_y$. In fact, the power spectrum reveals an approximate proportionality of the intrinsic period of oscillation, $T_0 \equiv f_0^{-1}$, with domain size, $L_y$, that is,

$$T_0 = f_0^{-1} = L_y/c\,, \tag{2}$$

where the proportionality constant $c \approx 2{\cdot}10^3\, km\, d^{-1}$. We further note that, in the case of RCE, the power spectrum is clearly dominated by a single peak for the smaller domain sizes $L_y = 10^3$ km and $L_y = 2 \cdot 10^3$ km, whereas for the larger $L_y$ also secondary peaks emerge.

Let us now turn on the surface temperature diurnal cycle, which is mimicked by a prescribed 5K-amplitude temporal temperature oscillation. Starting from the same initial condition as the corresponding RCE cases (Fig. 1a—d) the analysis period is thereby re-run for each of the four settings of $L_y$ (Fig. 1f—i). When examining the timeseries in f—i a striking finding is that the curve corresponding to $L_y = 8 \cdot 10^3$ km is all but unchanged, when comparing to its RCE counterpart (Fig. 1d). In fact, even the detailed dynamics of the curve is essentially preserved and diurnal perturbations are hardly visible. This qualitative finding is supported by the power spectrum, with only a marginal secondary peak appearing at $f_0 = 1\, d^{-1}$ for $L_y = 8 \cdot 10^3 km$ and the main features near $f_0 = .4d^{-1}$ and $.3d^{-1}$ mostly preserved. For $L_y = 4 \cdot 10^3 km$ the primary peak (near $.5d^{-1}$) is also preserved, however at a larger relative reduction. Conversely, a relatively large secondary peak at $f = 1d^{-1}$ appears. For $L_y = 2 \cdot 10^3 km$ the primary peak (near $.95d^{-1}$) is strongly diminished and almost entirely replaced by a sharp peak at $f_0 = 1d^{-1}$. For the smallest domain size, $L_y = 1 \cdot 10^3 km$, the trend is again reversed, with the primary peak near $f = 1.8d^{-1}$ mostly preserved and a more moderate peak near $f = 1d^{-1}$ appearing. Thus it seems that the larger the domain size $L_y$, the less the overall flow is impacted upon by diurnal perturbations — the large scales carry essentially all predictability, up to weeks ahead.

It is also interesting to examine the amplitude of oscillation for the timeseries $R(t)$ corresponding to different values of $L_y$. It is clear that the case of $L_y = 2{\cdot}10^3 km$ stands out, when the diurnal cycle is imposed, with the amplitude nearly doubling, as compared to its RCE counterpart. The case of $L_y = 4 \cdot 10^3 km$ also shows a significant increase in amplitude, however it should be considered that there is substantial internal variability, which could affect this finding. Overall these results suggest that the effect of the diurnal cycle is not linearly dependent on the domain size $L_y$. Rather, its effect seems to be most pronounced, when the intrinsic frequency matches that of the diurnal cycle, that is $f_0 \approx 1d^{-1}$ — suggesting a form of resonance mechanism.

Examining the change in $\overline{R}$ with domain size $L_y$ it is now apparent that $\overline{R}$ increases monotonically with $L_y$. Since the spatial temperature variance is now equal in all simulations (in contrast to Fig. S1), we here attribute the increase in $\overline{R}$ to more pronounced segregation into a narrowing convective ITCZ-like region near the "equator," which is surrounded by predominantly subsiding sub-regions.

### 3.2 Meridional mode

To more closely explore the mechanisms, we now examine the case of $L_y = 2 \cdot 10^3$ km to characterize the dynamical features of the resonance, as seen in domain mean precipitation. To reduce the internal inter-day variability, we focus on a "composite period" of the precipitation oscillations. We define such a composite by first detecting the time points of all local maxima and minima from the domain mean precipitation timeseries (Fig. S2). We then use the timepoint of each minimum to define the zero of a repeated cycle. The timepoint of the subsequent maximum is used as the turning point within the cycle and the subsequent minimum is used to define the cycle's period. By combining such data from each of the cycles available, we compute composite quantities, such as the composite cycle of domain mean precipitation intensity (Fig. 2). The comparison of RCE and DIU confirms that the period for RCE is slightly longer than one day ($\approx$ 1.05d), whereas it equals one day for DIU, and that the amplitude of composite precipitation intensity for RCE is much more modest than for the case of DIU. Notably, for DIU the mean precipitation intensity all but reaches zero for the minima, whereas its period maximum far exceeds that for the RCE case.

Variations in domain mean precipitation typically imply changes in the large-scale circulation. We characterize the large-scale circulation by first performing a "zonal" mean, corresponding to an average along the $x$-coordinate direction. We then again perform the composite average described above for the different time points during the approximately periodic cycles. A trademark of fluctuations of the upper troposphere w.r.t. its mean state are gravity waves, which can e.g. be derived from the linearized shallow water equations for atmospheric pressure and horizontal wind (Kiladis et al., 2009). To capture the general dynamics of the intrinsic (RCE) pressure (or equivalently geopotential) fluctuations, we plot the meridional pressure within the mid troposphere ($z = 3.5\,km$) for each composite time point (Fig. 3a). The time sequence of the curves (red$\rightarrow$ purple$\rightarrow$ red) indicates a standing wave-like dynamics, with pressure maxima traveling between the "equator" ($y = 0$) and the "subtropics" in the course of one period. Comparing the corresponding meridional rain rates (Fig. 3e), it is found that times of low precipitation (red curves) correspond to local equatorial pressure maxima, whereas high rain rate correspond to local pressure minima.

The meridional mid-tropospheric wind, $v(3.5\,km)$, as well as that near the surface, $v_{srf}$, is predominantly directed towards the equator, e.g., $v(3.5\,km) > 0$ and $v_{srf} > 0$ for $y < 0$. Cloud-base meridional wind, $v(1.3\,km)$ shows a more variable dynamics, with outflows during times of weak rain rates but inflows during times of heavy rainfall. From continuity, the latter implies outflows for the upper troposphere.

Turning to DIU, qualitative changes occur: the mid-tropospheric pressure field varies more strongly in time, but loses some of the meridional dependence found for RCE. Qualitative changes are also visible in $v(3.5\,km)$, where inflows into the equatorial regions are weakened and reverse to become outflows during times of pronounced rainfall.

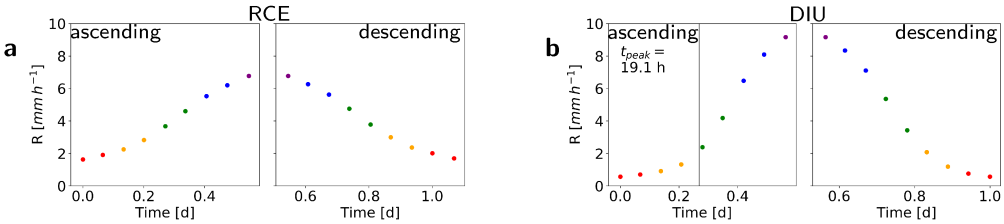


**Figure 2. Composite precipitation diurnal cycle.** The composite was obtained by collecting maxima and minima in the respective timeseries (*compare*: Fig. S2) and separating ascending and descending sections of each oscillatory period. **a**, RCE, $L_y = 2{,}000$ km **b**, DIU, $L_y = 2{,}000$ km

### 3.3 Conceptual model

To capture the domain mean dynamics of the different simulations, we propose a simple, qualitative, toy model with the following basic ingredients: We consider that the atmosphere undergoes periodic forcing due to the imposed diurnal cycle of period $T_d = f_d^{-1} = 2\pi\Omega^{-1} = 1\,d$. We capture all damping effects, such as surface drag and viscous dissipation, within a damping parameter $b$. Further, the atmosphere also shows an intrinsic oscillatory mode. In line with standing linear gravity wave theory (Yamagata & Hayashi, 1984; Yang & Ingersoll, 2013; Yang, 2021) and the results shown in Fig. 3, we assume the period of this mode, $T_0 = f_0^{-1} = 2\pi\omega_0^{-1}$, to increase approximately linearly with domain size $L_y$. The fundamental gravity wave speed is thereby assumed to be approximately independent of $L_y$. Our model simplifies further compared to the recent literature (Yang & Ingersoll, 2013; Yang, 2021): whereas Yang (2021) retain dynamics along one spatial dimension, our starting point is to assume that convection is strongly localized (pointlike) to the model ITCZ and the dynamics can thus be treated as an ordinary differential equation. Our primary model variable, $y(t)$, represents some measure of convective instability, e.g., low-level moisture convergence. A value of $y = 0$ will therefore be used to represent the activation of convection. We further idealize by assuming the convective timescale to be very short compared to the period of the standing gravity waves, and treat convection as a discrete Dirac delta signal (or $\delta$-pulse). In addition, the model allows for a diurnal forcing, which we simply incorporate as a sinusoidal drive of amplitude $A$. We now first introduce the linear model, where convection does not feed back on circulation. We then describe the non-linearity introduced by convective heating.

**Linear driven harmonic oscillator.** Together with the diurnal forcing, the linear model is that of a damped harmonic oscillator, namely:

$$y'' + 2b\,y' + \omega_0^2\,y = Ae^{i\Omega t}\,, \tag{3}$$

where primes denote temporal derivatives. As is well known, e.g., from Serway and Jewett (2018), for the steady state one can make the ansatz that

$$y(t) = y_0 e^{i(\Omega t + \phi)}\,, \tag{4}$$

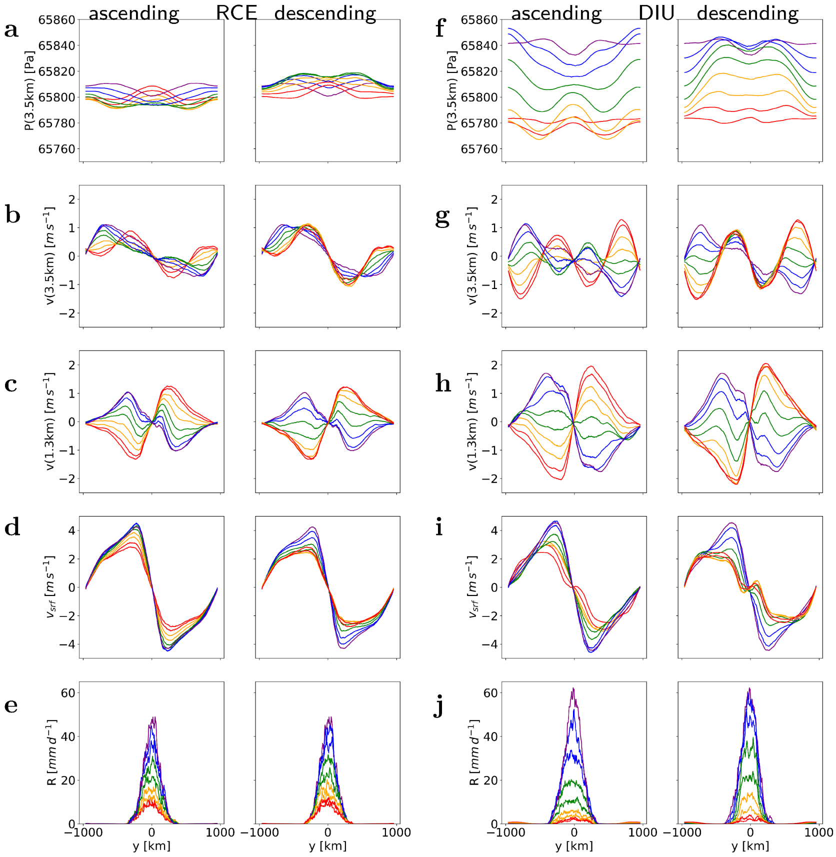


**Figure 3. Meridional oscillatory mode. a—e**, All panels show zonally-averaged quantities for simulations corresponding to RCE for $L_y = 2,000$ km. The panels from (a) to (e) show pressure at 3.5 km height, meridional velocity $v$ at 3.5 km, 1.3 km and 50 m height, as well as the precipitation rate. Paired panels correspond to the ascending and descending precipitation intensity branches, respectively (as labeled on top of panels). **f—j**, Simulations corresponding to DIU, otherwise analogous to (a)—(e).

where $y_0$ is the amplitude of oscillation and $\phi$ the phase shift between the forcing and the response. Inserting Eq. 4 into Eq. 3 yields the well-known relation between the amplitude of oscillation, $y_0$, and the driving amplitude $A$,

$$y_0 = A \left( (\Omega_0^2 - \omega^2)^2 + (2b\omega)^2 \right)^{-1/2} . \tag{5}$$

Notably, $y_0$ achives a maximum $y_0^* = A \left( 2b\sqrt{\omega_0^2 - b^2} \right)^{-1}$, often called a resonance, when $\Omega = \Omega^* \equiv \sqrt{\omega_0^2 - 2b^2}$. The phase shift $\phi$ can be computed as

$$\phi = \arctan \frac{2b\Omega}{\Omega^2 - \omega_0^2} \tag{6}$$

and will approach $\phi^* = \pi/2$ at the resonance frequency $\Omega^*$, meaning that forcing and feedback are phase-lagged by a quarter period.

Importantly, the model in Eq. 3 has several qualitative shortcomings in describing the data at hand (Fig. 1): (i) the response $y(t)$ has the same, unique, frequency $\Omega$ as the forcing and is only shifted in phase relative to the forcing; (ii) in the large-$t$ limit the function $y(t)$, in the absence of a forcing frequency $\Omega$, $y(t)$ should approach a constant. Both outcomes (i) and (ii) are not found in the data. Rather: oscillations are present even under the absence of a periodic forcing (RCE, Fig. 1a—e) and the dynamics of the response does not generally adjust to the forcing frequency (Fig. 1f—j).

**Nonlinear model including convective drive.** We thus modify the Eq. 3 by allowing for a convective forcing that depends on the state of the circulation, $y(t)$. This convective forcing is modeled as a fixed momentum source, $\Delta v$, that is applied whenever moist air masses converge near the equator, i.e., when $y(t) = 0$. The convergence of moist air masses is associated with convective updrafts which in turn give rise to tropospheric heating and subsequent free tropospheric divergence, thus accelerating the circulation.

Eq. 3 is thus modified to take the form

$$\begin{aligned} y' &= v\,, & (7)\\ v' &= -2bv - \omega_0^2 y - Ae^{i\Omega t} + \underbrace{v\,\delta(y)\Delta v}_{B(y,v)}\,, & (8) \end{aligned}$$

where we have re-written the second order equation as two first order equations and added the term $B(y,v)$ to account for a spatially-dependent energy input. $B(y,v)$ has the effect of "boosting" the current velocity by the increment $\Delta v$, a process reminiscent of that in the "kicked rotor" (Chirikov, 1979). The factor of $v$ arises due to the change of variables in

$$\delta(y(t)) = \frac{\delta(t-t_0)}{dy/dt(t_0)} = \frac{\delta(t-t_0)}{v(t_0)}\,, \tag{9}$$

where $t_0$ is the time of zero crossing. $\Delta v \geq 0$ is a constant, controlling the "boost" received by the oscillator upon crossing the origin. Notably, by applying the signed value of $v$, the boost always occurs to reinforce the direction of travel.

$B(y,v)$ implicitly depends on time through the constraint that $y(t) = 0$. Eq. 3 could hence be augmented to read

$$y'' + 2b\,y' + \omega_0^2\,y = Ae^{i\Omega t} + \sum_n \delta(t-t_n)sgn(y')\Delta v\,, \tag{10}$$

where the times $t_n$ are determined by the condition $y(t_n) = 0$. As a linear equation, the fundamental solution to the LHS of Eq. 10 could be used to integrate the dynamics within any time interval $[t_n, t_{n+1}]$. It is thus to be expected that the solution to Eq. 10 be a superposition of oscillations at frequencies $\omega_0$ and $\Omega$.

**Mimicking RCE.** Consider first the case where the time dependent forcing is switched off, that is, $A = 0$. In this case, the set of equations in Eq. 8 represents piece-wise homogeneous ODEs, since the abrupt "boost" is only applied upon each zero crossing. For a given zero crossing, where $y = 0$, we can thus obtain the transient solution to Eq. 8 by assuming a given initial velocity at $t_0 = 0$, where we take the subscript to number zero crossings. Let us further assume that $b > 0$, such that energy can always be dissipated as some finite rate. An initial velocity $v(t_0 = 0) = v_0$ can be enforced by imposing the time-dependent forcing $f(t) = v_0\delta(t_0)$. The transient response of Eq. 8 is then the solution to

$$y'' + 2by' + \omega_0^2 y = v_0\delta(t_0)\,, \tag{11}$$

which is the fundamental solution

$$y(t) = v_0\frac{e^{-bt}}{q}\sin(qt) \tag{12}$$

where $q \equiv \sqrt{\omega_0^2 - b^2}$ is the intrinsic frequency under the damping $b$. For the under-damped case $\omega_0 > b$, thus $q \in \mathbb{R}$, the fundamental solution therefore represents a sinusoidal oscillation of constant period $2\pi q^{-1}$ which is exponentially damped at a rate $b$. Since the change of amplitude does not affect the period, we can compute the time of first zero crossing, that is, $t_1 = \pi/q$. With the velocity,

$$v(t) = \frac{dy(t)}{dt} = \frac{v_0}{q}e^{-bt}\left[-b\sin(qt) + q\cos(qt)\right] \tag{13}$$

the velocity at $t = t_1$ becomes

$$v(t_1) = v_0 e^{-bt_1} = -v_0 e^{-\pi b/q}\,, \tag{14}$$

since $y(t_1) = 0$ and $\cos(qt_1) = -1$.

At the time $t_1$ the "boost" $\Delta v$ will be applied, leading to the modified velocity

$$v(t_1) \rightarrow v(t_1) - \Delta v\,. \tag{15}$$

Noting that upon each zero crossing the sign of $v$ is reversed, we can simplify the notation by working only with the magnitude of $v$. The Eq. 15 then reads

$$|v(t_1)| = |v_0| r + \Delta v \tag{16}$$

where we define $r \equiv e^{-\pi b/q}$ as the amplitude decay during each period. Since the period of the fundamental solution (Eq. 12) is independent of the initial velocity, we can immediately compute the velocity at the second zero crossing, namely

$$|v(t_2)| = |v(t_1)| r + \Delta v \tag{17}$$

where $t_2 = 2\pi/q$. And thus for the n'th zero crossing,

$$\begin{aligned} |v(t_n)| &= |v(t_{n-1})| r + \Delta v && (18)\\ &= (|v(t_{n-2})| r + \Delta v) r + \Delta v && (19)\\ &= |v_0| r^n + \Delta v \sum_{m=0}^{n-1} r^m && (20)\\ &= |v_0| r^n + \Delta v \frac{1-r^n}{1-r}\,. && (21) \end{aligned}$$

In the steady state we can assume the limit $n \rightarrow \infty$, thus

$$|v(t_n)| = \frac{\Delta v}{1-r} = \frac{\Delta v}{1-e^{-\pi b/q}}\,, \tag{22}$$

since $\lim_{n\rightarrow\infty} r^n = 0$ for $r < 1$. Hence, after a sufficiently long transient time the oscillator will be independent of the initial condition and its dynamics will be determined by the "boost" $\Delta v$ as well as the system parameters, which enter $r$. In particular, in the limit $r \rightarrow 1$, $r < 1$, for the special case of zero damping, the amplitude of oscillation, will diverge.

For small damping, that is, $\pi b/q \ll 1$, the exponential can be expanded to first order, yielding

$$|v(t_n)| = \frac{\Delta v\, q}{\pi b} + \Delta v\, \mathcal{O}\left(\left(\frac{q}{\pi b}\right)^2\right)\,, \tag{23}$$

thus, the steady-state speed at the time of any zero crossing will increase proportionately with the the "boost" $\Delta v$, intrinsic frequency $q$ and inverse damping $b^{-1}$. Notably, in this case of $b \rightarrow 0$, the maximum amplitude $y_{max}$ reached between any two zero crossings (Eq. 12) approaches

$$y_{max} = \frac{\Delta v}{\pi b}\,, \tag{24}$$

a value that does depend on the "boost" $\Delta v$ and the damping $b$, but is independent of the intrinsic frequency $q$.

To exemplify the dependence on the parameters we simulate the timeseries for different parameter combinations until a steady state is reached (Fig. 4). Indeed, as illustrated (Fig. 4a), the maximal displacement from the origin is visually proportional to $\Delta v$, whereas this maximum displacement does not depend noticeably on $f_0$ (Fig. 4b).

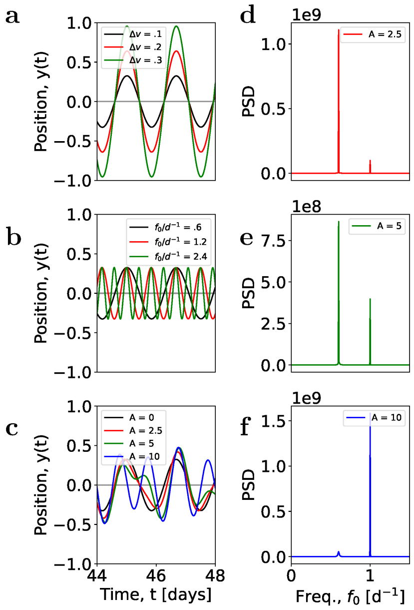


**Figure 4. Examples of timeseries simulated by the conceptual model.** Numerical simulations of Eq. 8 where the default parameters (shown as black curves in panels a—c) are chosen as $b$=.1, $f_0$=.6 $d^{-1}$, $A$=0, $\Delta v$=.1. Note that the parameters are chosen such as to represent the under-damped limit, here $\pi b/q \approx .09$. **a**, Varying $\Delta v$ (*see* legend); **b**, Varying $f_0$ (*see* legend); **c**, Varying $A$ (*see* legend); **d**—**f**, Power spectral density corresponding to the three finite-$A$ timeseries in (c) as labeled in the legends.

At this stage we have a separate understanding of (a) the dynamics of the temporally forced harmonic oscillator alone ($\Delta v = 0$), which performs oscillations at a frequency equal to that of the harmonic driving force, $\Omega$, at amplitude $y_0$ (Eq. 5) and (b) the spatially-forced non-linear oscillator ($A = 0$), which performs steady-state oscillations at the intrinsic system frequency $\omega_0$ and has an amplitude determined by the "boost" $\Delta v$.

**Mimicking DIU.** Allowing both $\Delta v > 0$ and $A > 0$ joins the two types of oscillators into one model. As mentioned, we expect some superposition of oscillations at frequencies $\omega_0$ and $\Omega$, yet, the relative weight of these two frequencies, the resultant phase shift $\phi$ or the joint amplitude of oscillation are less obvious. To provide examples, we simulate the previous timeseries, however now allowing for varying values of $A > 0$ (Fig. 4c). To implement the contribution from $B(y, v)$ numerically, we keep track of the value of the previous value of $y$ in the time integration routine. In the event that a change of sign in $y$ is detected, we apply a single increment of $\Delta v$ to the value of $v$, that is,

$$v \to v + sgn(v)\Delta v\,, \tag{25}$$

which ensures that the discrete quantity $\Delta v$ is applied to increment $v$. Noticeably, when $A = 2.5$ is chosen, some departure from the purely sinusoidal oscillation of the reference case is visible. For even larger values of $A$, additional oscillations appear and for $A = 10$ the timeseries is dominated by almost perfect one-day oscillations. The contributions from the different underlying frequencies can be quantified by evaluating the power spectrum of the respective timeseries (Fig. 4d—f), where the initial peak at $f_0 = .6\,d^{-1}$ gradually disappears as $A$ is increased.

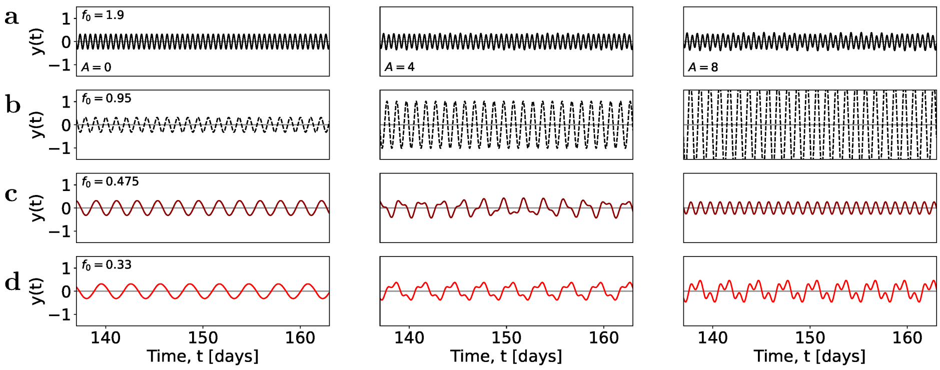


**Figure 5. Examples of timeseries simulated by the conceptual model for finite $A$ and varying $f_0$.**

To summarize the parameter space, the system is dependent on the intrinsic frequency $\omega_0$, the forcing frequency $\Omega$, the forcing amplitude $A$, the boost strength $\Delta v$ as well as the damping $b$. To simplify the analysis, we use $\Omega$ as the unit frequency, since it is set by the natural period of the diurnal forcing. We thus keep $\Omega$ fixed and will express $\omega$ in units of $\Omega$. We will further work in the limit of small $b \ll \omega_0$, such that oscillations decay slowly w.r.t. a single period of oscillation. We are thus only left with three remaining flexible parameters: the intrinsic frequency $\omega_0$, the forcing amplitude $A$ and the boost strength $\Delta v$.

We now aim to re-enact the numerical experiments (Fig. 1) for our simple conceptual model (Fig. 5) by step-by-step reducing the value of the parameter $f_0$, (a)—(d) in Fig. 5, which corresponds to increasing system sizes $L_y$ in Fig. 1. The first column corresponds to ($A = 0$), whereas the second and third columns corresponding to $A = 4$ and $A = 8$, respectively. As expected, the numerical results show that the period of oscillation increases linearly with $f_0^{-1}$ for the $A = 0$ case. For $A = 4$, variations in the timeseries occur, which qualitatively depend on the intrinsic frequency $f_0$: for the highest frequency ($f_0 = 1.9\,d^{-1}$), some modulations of the timeseries are visible, yet, the general shape of the timeseries is preserved, with the number of zero crossings unchanged and the amplitude very similar to the case of $A = 0$. A stark contrast however is visible for $f_0 = .95\,d^{-1}$, where the amplitude clearly increases, as does the number of zero crossings. Observing the number of zero crossings it is in fact apparent, that they now occur at the diurnal rate, $f = 1\,d^{-1}$. For the lower frequency cases ($f_0 = .475$ and $f_0 = .33$) the impact of the diurnal forcing is again much more modest, with the amplitude remaining similar to that of the $A = 0$ case, and the number of zero crossings remaining unchanged. Increasing the forcing even further ($A = 8$, third column), there is more disruption for all curves, yet, again, the case of $f_0 = .95$ undergoes a strong increase in amplitude, whereas the amplitude changes little in the other cases. However, the number of zero crossings for $f_0 = .475$ now adjusts to coincide with a diurnal rate. The even lower frequency case of $f_0 = .33$ continues to resist the "takeover" by $\Omega$ as the dominant frequency, albeit substantial disruptions are now evident.

Returning to Fig. 1, many parallels are indeed evident: The "resonant" case of $L_y = 2 \cdot 10^3\,km$, with intrinsic frequency $f_0 \approx .95$ also there reacts most strongly to the diurnal forcing, showing a strong increase in amplitude and an almost complete shift in dominant frequency to $f = 1\,d^{-1}$. The cases of higher and lower frequency tend to resist the impact of the diurnal forcing, with much more moderate impacts on the timeseries, e.g., little changes in amplitude or changes in the dominant frequency. In particular, for the lowest-frequency case of $L_y = 8{\cdot}10^3\,km$, the timeseries remains essentially unmodified when the diurnal cycle is applied (Fig. 1j). Further, the model reproduces the interference between the domain intrinsic and diurnal modes (*compare* timeseries Fig. 1i and Fig. 5d-right) which aliases the signal.

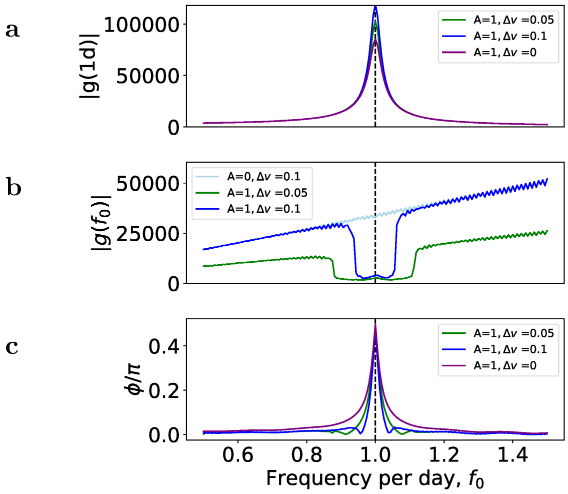


**Figure 6. Resonance for the toy model.** Damping $b = .1$. **a**, Power spectral density $|g(1d^{-1})|$, that is, the spectral weight corresponding to oscillations at the diurnal frequency, as a function of the intrinsic frequency $f_0$. Note the resonance near $f_0 = 1d^{-1}$ and the increase of the resonance for larger values of $\Delta v$. The curve for $\Delta v = 0$ (*see* legend) corresponds to the amplitude for the classical harmonic oscillator, as a function of the intrinsic frequency $f_0$. **b**, Spectral weight $|g(f_0)|$, that is, the weight corresponding to oscillations at the frequency $f_0$. The curve for $A = 0$ (light blue, *see* legend) corresponds to the special case without periodic forcing ($A = 0$) where $|v(t_n)| \sim q \approx f_0$ (Eq. 23), i.e., the spectral weight increases linearly with the intrinsic frequency. Note the dip near $f_0 = 1d^{-1}$, when $A > 0$. **c**, Phase lag between forcing frequency and response $y(t)$ for the classic harmonic oscillator (purple curve) and the cases where $\Delta v > 0$.

In Fig. 6 we summarize the model findings by plotting the spectral weight $|g(f)|$ for $f = 1d^{-1}$ (panel a) as well as for $f = f_0$ (panel b) as a function of the intrinsic frequency $f_0$. The curve for $|g(1d^{-1})|$ equals that of the classical harmonic oscillator amplitude for $\Delta v = 0$, with a pronounced resonance near $f_0 = 1d^{-1}$, which diverges for $b = 0$ (*compare*: Eq. 5). For increasing $\Delta v > 0$, the resonance is further increased. The $f_0$ dependence of $|g(f_0)|$ is more complex: as expected, in the limiting case of $A = 0$ the spectral weight increases approximately linearly with $f_0$ (Eq. 23). However, when a periodic forcing is applied, i.e., $A > 0$, a region of suppressed $|g(f_0)|$ appears in the vicinity of $f_0 = 1d^{-1}$. This suppressed region appears to grow when $\Delta v$ is diminished, such that for $\Delta v \to 0$ we expect the diurnal cycle to entirely dominate the dynamics. Conversely, for $\Delta v \to \infty$, the slope of the curve for $A = 0$ diverges and we expect the suppressed region to vanish and the intrinsic frequency to entirely dominate the dynamics. Finally, we also plot the phase lag between the forcing and the position $y(t)$ (Fig. 6c), which again contrasts the classical harmonic oscillator to the mixed oscillator. The main finding is that the phase lag disappears more quickly away from the resonance frequency, when $\Delta v$ is increased.

## 4 Discussion and Conclusion

We have presented a suite of numerical simulations, which provide a highly simplified representation of the Hadley Circulation, including an intertropical convergence zone with a strongly localized latitudinal band of deep convection near the model equator. The simulations, which use horizontally cyclic boundary conditions but impose a meridional temperature gradient away from the equator, further feature a prominent self-organized oscillation in surface precipitation, thus deep convection, with a period $\omega_0 \sim L_y$, where $L_y$ is the meridional extent of our simulations. We attribute this oscillation to the emergent build-up of low wavenumber standing gravity waves, which sync with convective activity near the equator.

We then explore the crosstalk with the surface temperature diurnal forcing, the most dominant "pacemaker" of tropical convection. Such diurnal forcing is implemented by allowing for additional imposed temporal periodicity in the surface temperature forcing. Our simulations show that the diurnal cycle can interfere with the system intrinsic mode but does not dominates the resulting oscillations in surface precipitation. Indeed, only when $\omega_0$ lies in the vicinity of the diurnal frequency, does the diurnal frequency dominate the dynamics, and a resonance in rainfall intensity occurs. Otherwise, oscillations at $\omega_0$ dominate the power spectrum.

We propose a simple ordinary differential equation model to re-enact the convective precipitation dynamics: a simple harmonic oscillator is thereby augmented by a momentum "boost," applied whenever the oscillator crosses a threshold. The simple model explains the resonance near the diurnal frequency and the prevalence of $\omega_0$ far away from it. It demonstrates that, dependent on the intrinsic frequency $\omega_0$, the power spectrum can be dominated by $\omega_0$ or $\Omega$.

The diurnal cycle is a key element in tropical and mid-latitude rainfall and its understanding and proper representation in weather and climate models is still challenging. In particular, the relation between the diurnal cycle and the occurrence of extreme convective events, such as mesoscale convective systems, is of great importance, due to the implications for flooding (Tan et al., 2015; Schumacher & Rasmussen, 2020; Fowler et al., 2021).

The interplay between organized convection and the large scale circulation has fascinated the scientific community for decades (Lindzen, 1974; K. A. Emanuel, 1987; Neelin et al., 1987; Wang, 1988; Takayabu, 1994; Wheeler & Kiladis, 1999; Kiladis et al., 2009; Mapes, 2000; Majda & Shefter, 2001; Sobel & Bretherton, 2000; Härtel et al., 2000; Kuang, 2012; Yang & Ingersoll, 2013; Yang, 2021). Our phenomenological model builds on the existence of low-wavenumber standing gravity waves and helps understand how the diurnal cycle interferes with such waves. The standing fundamental modes have been reported to self-organize when convection aggregates and eventually "singles out" such system-scale oscillations. While promising suggestions exist (Yang & Ingersoll, 2013; Yang, 2021), building further evidence on how such modes come about within a coupled, self-organized process, should provide the community with deeper understanding of convectively coupled equatorial waves.

## Acknowledgments

The authors gratefully acknowledge funding by a grant from the VILLUM Foundation (grant number: 13168) and the European Research Council (ERC) under the European Union's Horizon 2020 research and innovation program (grant number: 771859) and the Novo Nordisk Foundation Interdisciplinary Synergy Program (grant no. NNF19OC0057374). This work used resources of the Deutsches Klimarechenzentrum (DKRZ), granted by its Scientific Steering Committee (WLA) under project ID bb1166.

## References

Bretherton, C. S., Blossey, P. N., & Khairoutdinov, M. (2005). An energy-balance analysis of deep convective self-aggregation above uniform SST. *Journal of the Atmospheric Sciences*, *62*(12), 4273–4292.

Chirikov, B. V. (1979). A universal instability of many-dimensional oscillator systems. *Physics reports*, *52*(5), 263–379.

Emanuel, K., Wing, A. A., & Vincent, E. M. (2014). Radiative-convective instability. *Journal of Advances in Modeling Earth Systems*, *6*(1), 75–90.

Emanuel, K. A. (1987). An air-sea interaction model of intraseasonal oscillations in the tropics. *Journal of Atmospheric Sciences*, *44*(16), 2324–2340.

Fowler, H. J., Lenderink, G., Prein, A. F., Westra, S., Allan, R. P., Ban, N., … others (2021). Anthropogenic intensification of short-duration rainfall extremes. *Nature Reviews Earth & Environment*, *2*(2), 107–122.

Haerter, J. O., Meyer, B., & Nissen, S. B. (2020). Diurnal self-aggregation. *npj Climate and Atmospheric Science*, *3*, 30.

Härtel, C., Carlsson, F., & Thunblom, M. (2000). Analysis and direct numerical simulation of the flow at a gravity-current head. part 2. the lobe-and-cleft instability. *Journal of Fluid Mechanics*, *418*, 213–229. doi: 10.1017/S0022112000001270

Held, I. M., Hemler, R. S., & Ramaswamy, V. (1993). Radiative-convective equilibrium with explicit two-dimensional moist convection. *Journal of the Atmospheric Sciences*, *50*(23), 3909–3927.

Jensen, G. G., Fiévet, R., & Haerter, J. O. (2021). The diurnal path to persistent convective self-aggregation. *arXiv preprint arXiv:2104.01132*.

Khairoutdinov, M. F., & Randall, D. A. (2003). Cloud resolving modeling of the arm summer 1997 iop: Model formulation, results, uncertainties, and sensitivities. *Journal of Atmospheric Sciences*, *60*(4), 607–625.

Kiladis, G. N., Wheeler, M. C., Haertel, P. T., Straub, K. H., & Roundy, P. E. (2009). Convectively coupled equatorial waves. *Reviews of Geophysics*, *47*(2).

Kuang, Z. (2012). Weakly forced mock walker cells. *Journal of the Atmospheric Sciences*, *69*(9), 2759–2786.

Lindzen, R. S. (1974). Wave-cisk in the tropics. *Journal of Atmospheric Sciences*, *31*(1), 156–179.

Majda, A. J., & Shefter, M. G. (2001). Models for stratiform instability and convectively coupled waves. *Journal of the atmospheric sciences*, *58*(12), 1567–1584.

Mapes, B. E. (2000). Convective inhibition, subgrid-scale triggering energy, and stratiform instability in a toy tropical wave model. *Journal of the Atmospheric Sciences*, *57*(10), 1515–1535.

Mlawer, E. J., Taubman, S. J., Brown, P. D., Iacono, M. J., & Clough, S. A. (1997). Radiative transfer for inhomogeneous atmospheres: Rrtm, a validated correlated-k model for the longwave. *Journal of Geophysical Research: Atmospheres*, *102*(D14), 16663-16682.

Muller, C., Yang, D., Craig, G., Cronin, T., Fildier, B., Haerter, J. O., … others (2022). Spontaneous aggregation of convective storms. *Annual Review of Fluid Mechanics*, *54*, 133–157.

Muller, C. J., & Held, I. M. (2012). Detailed investigation of the self-aggregation of convection in cloud-resolving simulations. *Journal of the Atmospheric Sciences*, *69*(8), 2551–2565. doi: https://doi.org/10.1175/JAS-D-11-0257.1

Müller, S. K., & Hohenegger, C. (2020). Self-aggregation of convection in spatially varying sea surface temperatures. *Journal of Advances in Modeling Earth Systems*, *12*(1), e2019MS001698.

Neelin, J. D., Held, I. M., & Cook, K. H. (1987). Evaporation-wind feedback and low-frequency variability in the tropical atmosphere. *Journal of Atmospheric Sciences*, *44*(16), 2341–2348.

Patrizio, C. R., & Randall, D. A. (2019). Sensitivity of convective self-aggregation to domain size. *Journal of Advances in Modeling Earth Systems*, *11*(7), 1995–2019.

Raymond, D. J. (2000). The hadley circulation as a radiative–convective instability. *Journal of the atmospheric sciences*, *57*(9), 1286–1297.

Schumacher, R. S., & Rasmussen, K. L. (2020). The formation, character and changing nature of mesoscale convective systems. *Nature Reviews Earth & Environment*, *1*(6), 300–314.

Serway, R. A., & Jewett, J. W. (2018). *Physics for scientists and engineers*. Cengage learning.

Shamekh, S., Muller, C., Duvel, J.-P., & D'Andrea, F. (2020). Self-aggregation of convective clouds with interactive sea surface temperature. *Journal of Advances in Modeling Earth Systems*, *12*(11), e2020MS002164. Retrieved from `https://agupubs.onlinelibrary.wiley.com/doi/abs/10.1029/2020MS002164` (e2020MS002164 10.1029/2020MS002164) doi: https://doi.org/10.1029/2020MS002164

Sobel, A. H., & Bretherton, C. S. (2000). Modeling tropical precipitation in a single column. *Journal of climate*, *13*(24), 4378–4392.

Takayabu, Y. N. (1994). Large-scale cloud disturbances associated with equatorial waves part i: Spectral features of the cloud disturbances. *Journal of the Meteorological Society of Japan. Ser. II*, *72*(3), 433–449.

Tan, J., Jakob, C., Rossow, W. B., & Tselioudis, G. (2015). Increases in tropical rainfall driven by changes in frequency of organized deep convection. *Nature*, *519*(7544), 451–454. doi: https://doi.org/10.1038/nature14339

Tompkins, A. M. (2001). Organization of tropical convection in low vertical wind shears: The role of water vapor. *Journal of the Atmospheric Sciences*, *58*(6), 529–545.

Tulich, S. N., Randall, D. A., & Mapes, B. E. (2007). Vertical-mode and cloud decomposition of large-scale convectively coupled gravity waves in a two-dimensional cloud-resolving model. *Journal of the atmospheric sciences*, *64*(4), 1210–1229.

Wang, B. (1988). Dynamics of tropical low-frequency waves: An analysis of the moist kelvin wave. *Journal of the atmospheric sciences*, *45*(14), 2051–2065.

Wheeler, M., & Kiladis, G. N. (1999). Convectively coupled equatorial waves: Analysis of clouds and temperature in the wavenumber–frequency domain. *Journal of the Atmospheric Sciences*, *56*(3), 374–399.

Wing, A. A., & Cronin, T. W. (2016). Self-aggregation of convection in long channel geometry. *Quarterly Journal of the Royal Meteorological Society*, *142*(694), 1–15.

Yamagata, T., & Hayashi, Y. (1984). A simple diagnostic model for the 30-50 day oscillation in the tropics. *Journal of the Meteorological Society of Japan. Ser. II*, *62*(5), 709–717.

Yamaguchi, T., Randall, D. A., & Khairoutdinov, M. F. (2011). Cloud modeling tests of the ultimate–macho scalar advection scheme. *Monthly Weather Review*, *139*(10), 3248–3264.

Yang, D. (2021). A shallow-water model for convective self-aggregation. *Journal of* *the Atmospheric Sciences*, *78*(2), 571–582.

Yang, D., & Ingersoll, A. P. (2013). Triggered convection, gravity waves, and the mjo: A shallow-water model. *Journal of the atmospheric sciences*, *70*(8), 2476–2486.

Zhang, C., Adames, Á., Khouider, B., Wang, B., & Yang, D. (2020). Four theories of the madden-julian oscillation. *Reviews of Geophysics*, *58*(3), e2019RG000685.

# Supporting Information for "Precipitation resonance for an idealized model ITCZ"

**Jan O. Haerter**[1,2,3] **and Romain Fiévet**[3]

[1]Complexity and Climate, Leibniz Center for Tropical Marine Research, Fahrenheitstrasse 6, 28359 Bremen, Germany
[2]Jacobs University Bremen, Campus Ring 1, 28759 Bremen, Germany
[3]Niels Bohr Institute, Copenhagen University, Blegdamsvej 17, 2100 Copenhagen, Denmark

**Contents of this file** This Supporting Information contains additional figures relevant for some specialist readers.

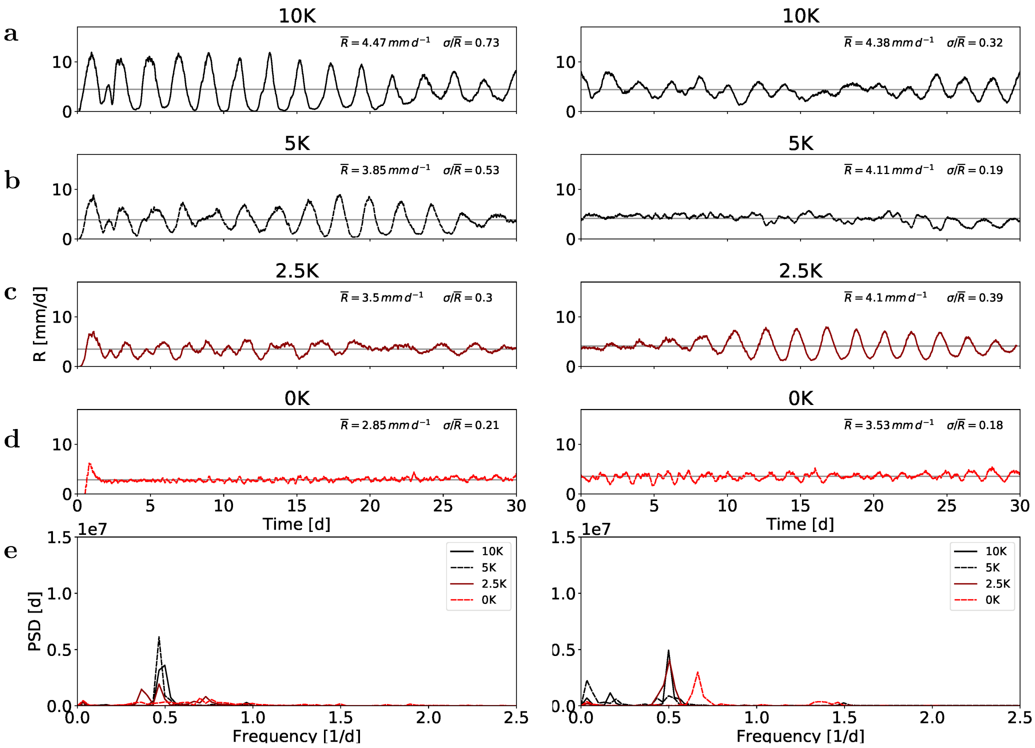


**Figure S1. Domain-mean precipitation for varying latitudinal temperature gradients.** Panels show timeseries of horizontal-mean surface precipitation intensity for latitudinal temperature differences $\Delta T_{s,lat} \equiv T(x, y = L_y/2, t) - T(x, y = 0, t)$ as labeled on top of each panel. The meridional domain size $L_y = 4000\,km$ in all simulations shown. Left and right stacks of panels correspond to the 30-day spinup and 30-day analysis periods, respectively. Note the substantial internal variability for all simulations and in particular the shift in power spectral density for $\Delta T_{s,lat} = 0K$.

Corresponding author: Jan O. Haerter, `haerter@nbi.ku.dk`

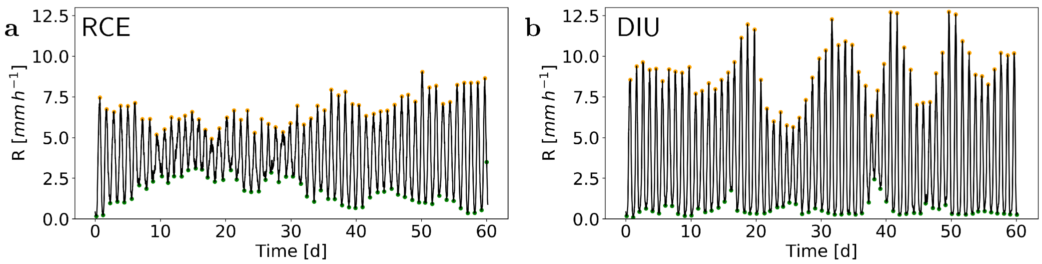


**Figure S2. Detecting timeseries peaks and minima.** Timeseries for domain mean surface precipitation $R(t)$ for RCE (shown in **a**) and DIU (panel **b**) for equal meridional domain size $L_y = 2,000\,km$. Detected peaks and minima are highlighted by orange and green symbols, respectively.